

EFFECT OF BUILD PARAMETERS AND BUILD GEOMETRIES ON RESIDUAL MICROSTRUCTURES AND MECHANICAL PROPERTIES OF Ti-6Al-4V COMPONENTS BUILT BY ELECTRON BEAM MELTING (EBM)

L. E. Murr,^{1,2} S. M. Gaytan,^{1,2} F. Medina², E. Martinez,^{1,2} D. H. Hernandez^{1,2} L. Martinez^{1,2} M. I. Lopez,^{1,2} R. B. Wicker^{2,3} and S. Collins⁴

¹Department of Metallurgical and Materials Engineering
The University of Texas at El Paso, El Paso, TX 79968 USA

²W. M. Keck Center for 3-D Innovation
The University of Texas at El Paso, El Paso, TX 79968 USA

³Department of Mechanical Engineering
The University of Texas at El Paso, El Paso, TX 79968 USA

⁴Arcam AB, Mölndal, Sweden

Reviewed, accepted 9/15/09

Abstract

In this study, involving additive manufacturing (AM) using electron beam melting (EBM), we have examined build defects which result from beam tripping, porosities (including unmelted or unsintered zones) due to excursions from optimal build parameters (especially variations in melt scan beam current and scan speed), and gas bubbles trapped in atomized Ti-6Al-4V starting powder as well as recycled powder, and retained in the build. At optimized build conditions we have also examined microstructure-mechanical property (hardness, tensile strength, and elongation) variations for multiple rake building and multiple melt scans using optical metallography and scanning and transmission electron microscopy (SEM and TEM). These build variances cause cooling rate variances which promote α -phase growth and variations in dislocation density, as well as α -to- α' (martensite) phase changes, all of which produce some degree of mechanical property variations. These features (especially α -to- α' phase changes) are notable on comparing solid builds in comparison with a variety of mesh arrays where strut dimension and build-element complexities alter the cooling rates in a significant way. We illustrate these microstructure variations with corresponding variations in microindentation hardness measurements made directly on fine mesh (strut) structures. Finally, we have examined Ti-6Al-4V powder chemistries and solid build chemistries which for single-pass melt scans at optimized build conditions are shown to be relatively constant up to 40 cycles of powder reuse with the exception of Al content which was reduced by 10 to 15% in solid builds at optimized conditions. However, Al loss in solid builds approached 25% for multiple (2 and 3) melt scans, while no changes in Ar gas-bubble density were observed with changes in α -phase (grain) width which increased from 3 μm for a single melt scan to 4.5 and 6 μm for 2 and 3 melt scans, respectively. Corresponding Rockwell C-scale (HR_C) hardness varied from 37, 36, and 35, respectively; with ultimate tensile strengths exceeding 1.2 GPa at elongations of 12% or higher for this melt scan sequence.

Introduction

The fabrication of complex, multifunctional, monolithic components is a particular advantage of solid freeform fabrication (SFF). For example, while biomedical devices can be machined from forged billets and proximal or total surface porosity developed by subsequent spray or sinter processes, it is impossible to join foam or mesh components of various kinds as an integral part of a monolithic device. Furthermore, metal mesh or foam structures are impossible to produce as an integral part of the conventional machining process, or any related manufacturing process except for foaming protocols in the melt, which do not work for Ti-6Al-4V and other high-temperature, reactive metals and alloys. Similarly, mesh or foam arrays for impact energy

management in aerospace and automotive applications are not conventionally tractable as well as numerous, related product configurations for thermal management (such as heat exchangers), sound adsorption and vibration suppression structures, and the like. However, additive manufacturing (AM) using laser or electron beams can build any complex, monolithic component through computer-controlled or computer-aided design (CAD) driven self-assembly by melting precursor powder layers. Unfortunately, these processes are not well certified in terms of manufacturing standards which are well documented for wrought or cast precursor manufacturing for Ti-6Al-4V in particular, and related alloy systems, although there has been some recent progress for EBM produced components (Wooten, 2008; Gaytan *et al.*, 2009).

In this research program, we have been concerned with optimizing the EBM build process and understanding microstructural and mechanical variations which accompany variations in build parameters and build geometries using Ti-6Al-4V precursor powder.

Methods and Procedures

Figure 1 illustrates the ARCAM (A2) EBM system and AM process (Gaytan *et al.*, 2009). Similar in concept to other electron optical devices, an electron beam is generated in an electron gun ((1) in Fig. 1.) and projected through a focusing lens (2) and subsequently rastered over the building layers of powder (3), first involving multiple scans (~11) at high rate and high current (~15,000 mm/s @ 30mA) to preheat the powder layer to 760° C, leveling to ~640° C, followed by an optimized melt scan at ~400 mm/s @ 6 mA. Varying either the scan rate or current as well as the imposition of multiple melt scans can have very noticeable effects on the efficiency of the build as well as the properties of the build; microstructure and mechanical properties. The mean or average powder size illustrated in the insert in Fig. 1 was roughly 30 μm. Consequently each nominal 100 μm thick melted layer corresponds to several (≥ 3) mean powder particle layers. The powder is gravity fed from cassettes ((4) in Fig. 1) and raked (5) across each melt layer. Multiple rake passes for each layer may also alter the build properties by more effectively filling layer interstices with smaller powder particles. Consequently, beam scan and current variances, melt scan variances and rake variances, can all have an effect on the build product and build efficiency. These were explored in this study.

The powder used in this study was Ti-6Al-4V ELI powder having a nominal composition of 6.04 percent Al, 4.05 percent V, 0.013 percent C, 0.07 percent Fe, 0.13 percent O, and <0.005 percent N and H; the balance Ti (in weight percent). The average powder particle diameter was ~30 μm as noted. We have analyzed the precursor powder in the SEM (a Hitachi S4800 field-emission SEM) utilizing an energy dispersive (X-ray) spectrometer (EDS) as well as recycled powder, and the builds themselves to observe elemental variations, especially volatilization of Al. While oxygen is detectable by EDS, the resolution is ≥ 0.5% (weight).

Microstructures of various builds, including mesh arrays and related geometries were examined by optical metallography by mounting selected sections or coupons which were ground, polished, and etched; using a solution consisting of 100 mL H₂O, 2.5 mL HF, and 5 mL HNO₃. Polished and etched specimens were also tested by microindentation hardness testing using a Vickers indenter at 25 to 100 gf loads (HV). Solid, fully dense monoliths were also tested by Rockwell C-scale hardness indentation, and selected samples were machined into tensile specimens and tested using an Instron 500 R tensile machine at a strain rate of $3 \times 10^{-3} \text{ s}^{-1}$,

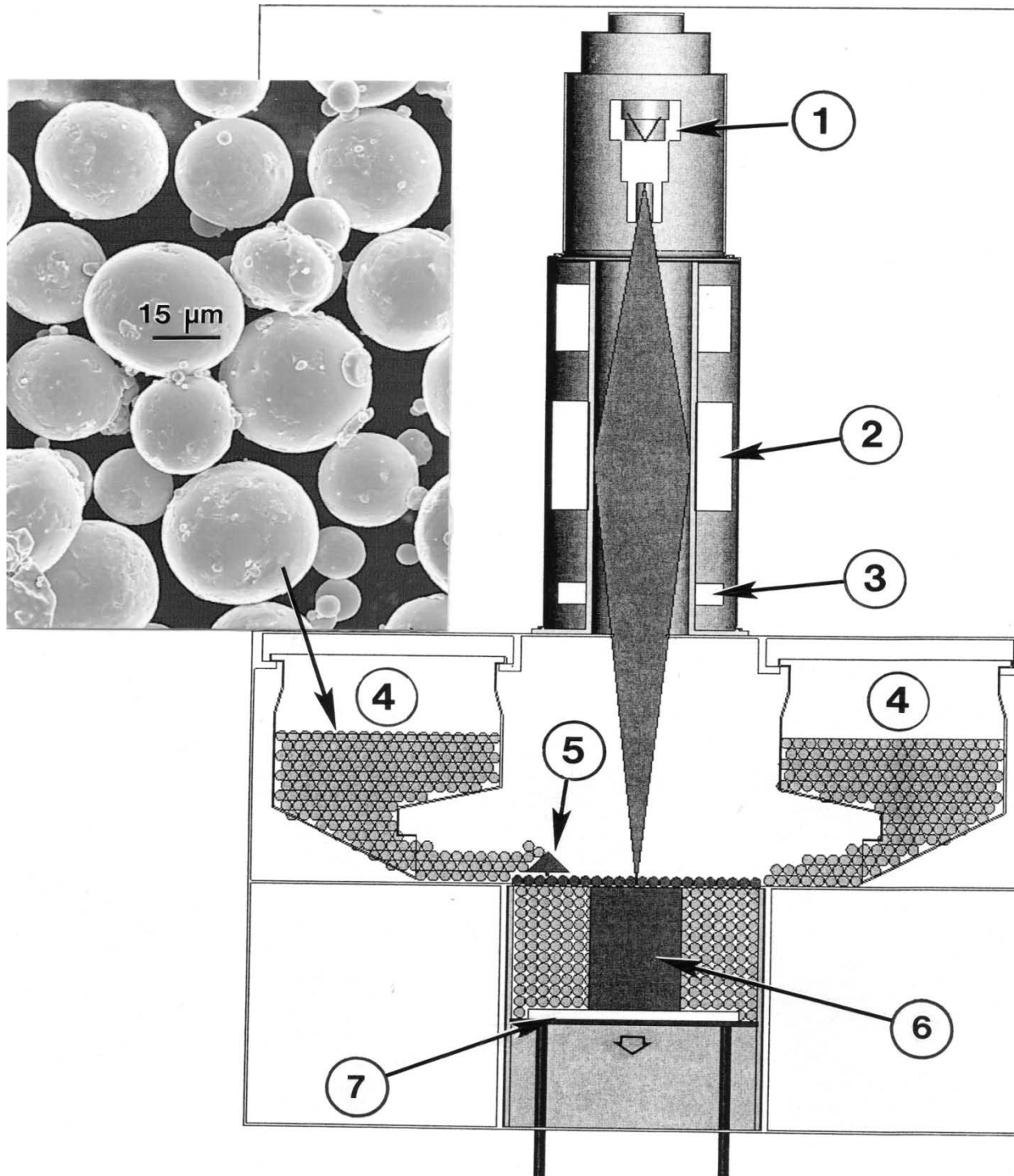


Figure 1. EBM schematic and SEM view of precursor powder (insert). Numbers denote the system components: (1) Electron gun, (2) Beam focus lens, (3) Beam deflection coils, (4) Powder cassettes, (5) Powder layer rake, (6) Build product, (7) Build table. From Gaytan, et al. (2009).

at room temperature ($\sim 20^{\circ}\text{C}$). HV and HRC values are nearly corresponding except for an order of magnitude or decimal place difference: $\text{HV} (\text{xxx}) \sim \text{HRC} (\text{xx.x})$.

We utilized techniques previously described in detail (Murr *et al.*, 2009a) to observe microstructures in builds by transmission electron microscopy. However, since we have recently demonstrated that mesh arrays and foams of Ti-6Al-4V fabricated by EBM exhibit variations in microstructure as a consequence of different cooling rates for small geometrical components such as mesh struts (Murr *et al.*, 2009b), we developed a novel build concept to examine these issues by TEM. Since it is not possible to prepare electron transparent thin sections for TEM from 1 mm or smaller struts, we developed a “test box” concept illustrated in Fig. 2. In this concept, 1 cm^2 window arrays having various thicknesses (ranging from 0.5 mm to 2 mm) are created along with 1 cm^3 solid sections for comparison (Fig. 2(b)). Standard 3 mm discs for TEM specimen preparation were then punched from these “windows” after grinding to ~ 0.2 mm thickness, including coupons cut from the solid test blocks (1 cm^3) in Fig. 2. These punched discs were electropolished as described previously (Murr *et al.*, 2009b), and examined in a Hitachi H-8000 analytical TEM operating at 200 kV accelerating potential, employing a goniometer-tilt stage. Similar “windows” in Fig. 2 were also mounted, polished, and etched for optical metallography in order that the macrostructure observed by optical metallography could be correlated with the TEM images. The hardness of “window” sections cut and mounted from Fig. 2(b) was also measured using a Vickers indenter (HV) as described previously. Several variations of this concept were pursued in order to achieve requisite cooling and cooling-rate variations.

Results and Discussion

Build Defects and Related Issues

There are notable build defects which can occur by improper layer filling, beam tripping which can involve momentary variations in beam energy or beam blanking. These involve poorly melted (or sintered) regions which can be considered porosity zones, and examples are illustrated in Figure 3. In addition, variations in optimized build parameters such as melt scan beam current or scan rate can also have deleterious effects on build integrity or build defects. Figure 4 illustrates this feature in the extreme by changing the melt scan beam current from the optimum of 6 mA to 1 mA. This creates an extremely porous and poorly consolidated build. Note the poorly sintered zone represented in Figure 4(b). This example also illustrates that it is not possible to build porous structures with any real integrity by simply changing melt scan rate or beam current.

We have examined the prospects for defects in builds depending upon whether the powder is raked one or more times for the creation of each layer. No statistically significant differences were observed on comparing a single rake pass with two (or three) rake passes, which is the preferred procedure for optimized builds. The reasoning is of course the fact that layer filling would be somewhat more complete for multiple rake passes. However, the Ti-6Al-4A powder illustrated in the insert in Figure 1 shows smaller particles sintered to larger ones, producing a bimodal particle size distribution as illustrated previously by Murr *et al.* (2009a). This may assure more consistent layer filling in contrast to unimodal particle size distributions.

Because the atomization process for manufacturing uniform, round Ti-6Al-4V particles traps argon gas bubbles, these bubbles are carried into the melt and retained in the solidified build as

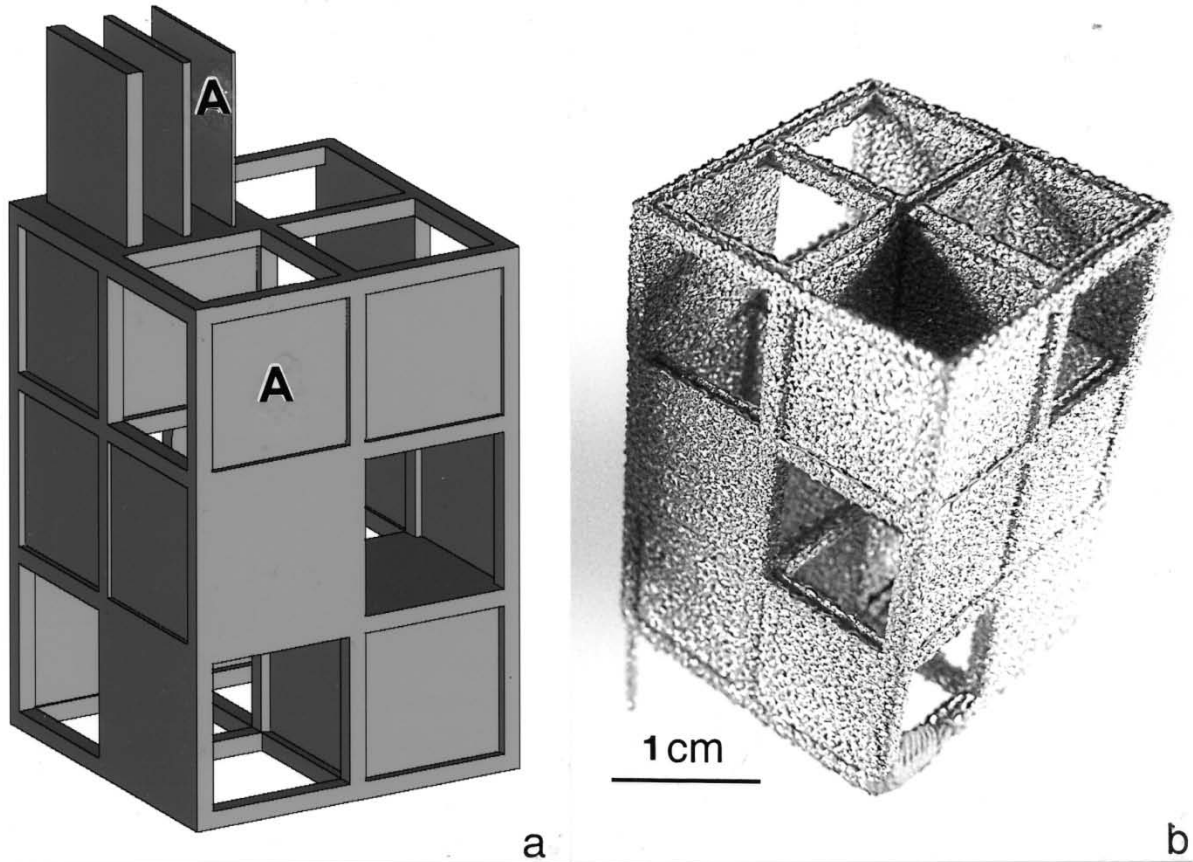


Figure 2. CAD model (a) and actual Ti-6Al-4V build prototype (b) for build “window” array concept. The windows or similar array components as shown at “A” in (a) or “windows” have varying thicknesses to produce varying cooling rates. These array components permit convenient characterization by optical microscopy and TEM. TEM requires 3 mm discs to be punched from the thinnest component (~ 0.2 mm) while thicker features are ground and polished to this thickness. The surface features in (b) are exaggerated by spectral reflectance.

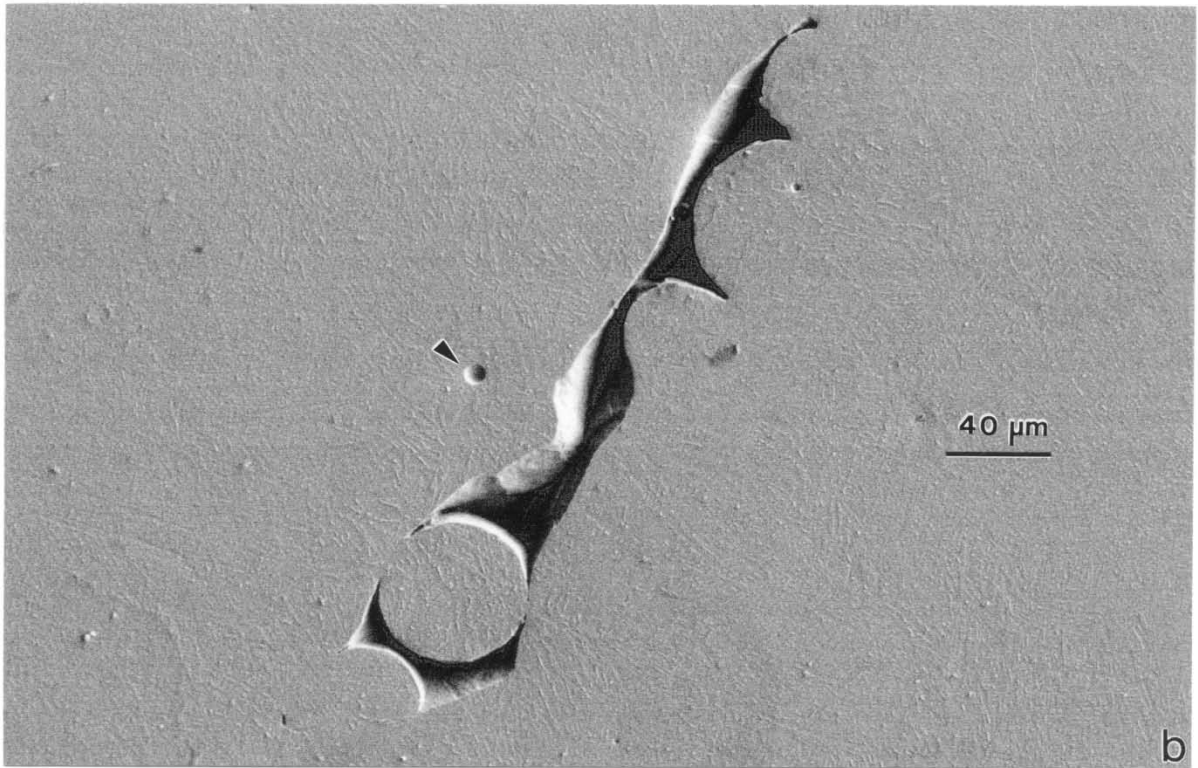
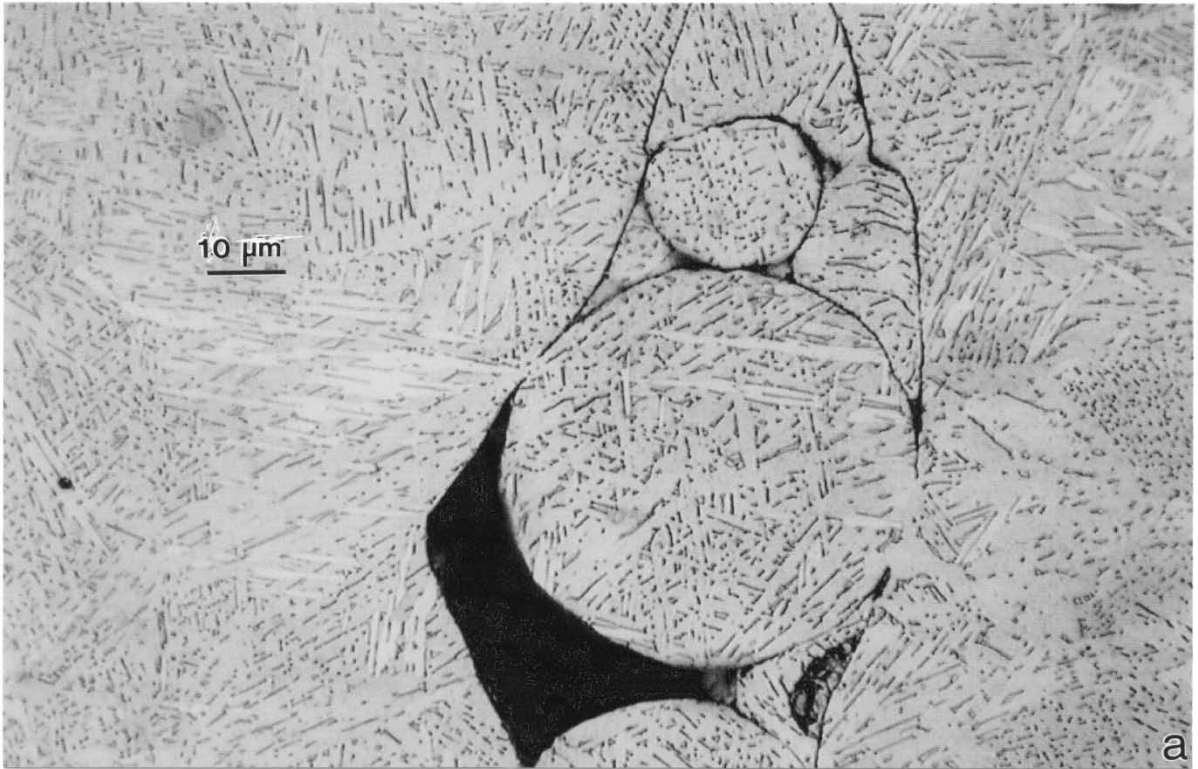


Figure 3. Examples of build defects. (a) Unmelted and consolidated zone. (b) is similar to (a) with gas void (exposed bubble) at arrow. From Gaytan, et al. (2009).

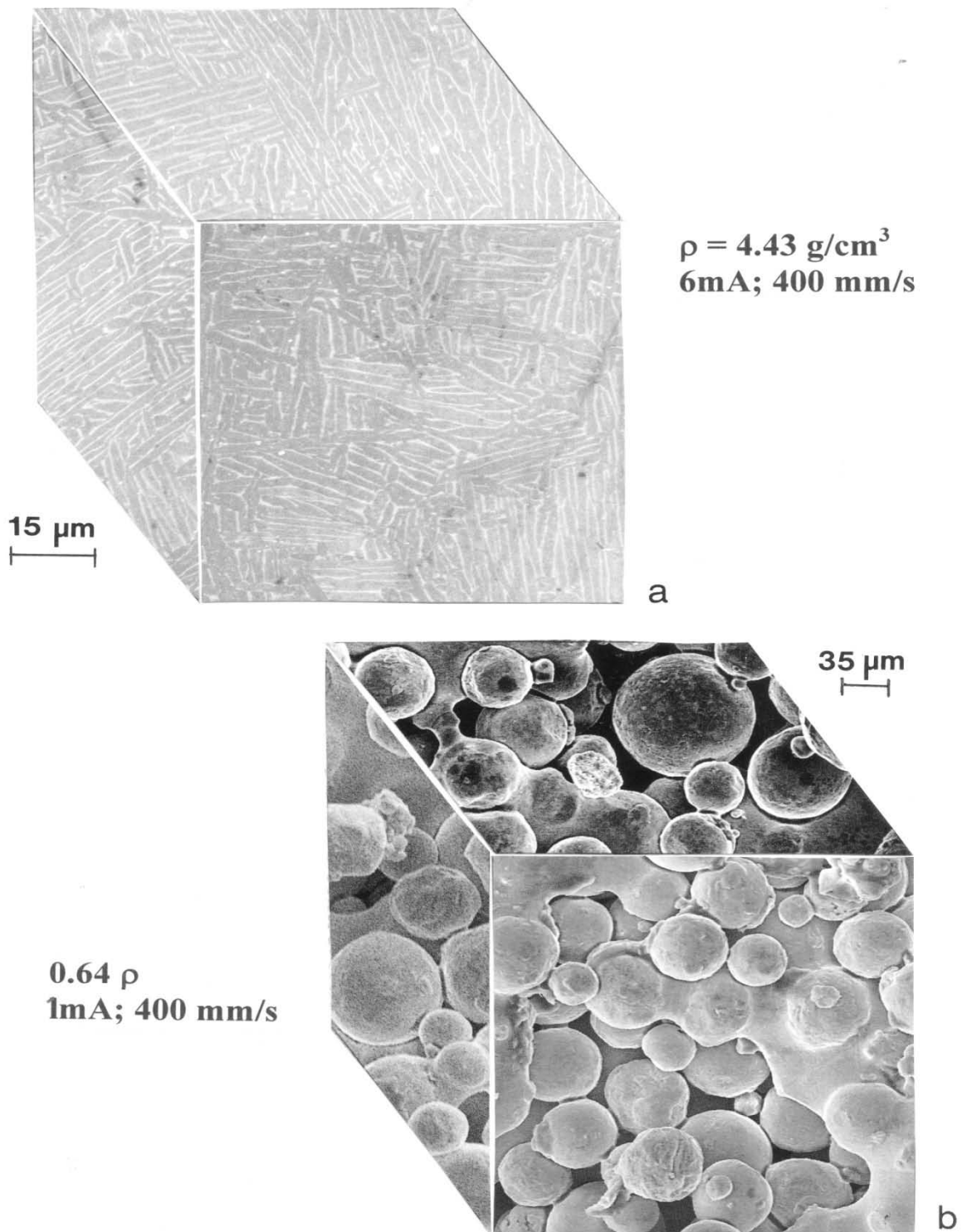


Figure 4. Ti-6Al-4V build comparisons. (a) Shows the optimized build parameters to produce fully dense monolith while (b) shows a reduction in melt-beam current. From Gaytan, et al., (2009).

illustrated in Figure 5 which shows retained argon bubbles which can range in size from $<10\ \mu\text{m}$ to $>50\ \mu\text{m}$ in diameter. The argon gas is apparently not under any significant pressure when trapped, and the high temperature of the melt ($\sim 1670^\circ\text{C}$) and the high surface tension of Ti-6Al-4V does not permit these bubbles to leave the melt. Figure 6 illustrates several typical examples of bubbles breaking out of the precursor powder particles, especially in the SEM view shown in Figure 6b.

As noted, the high melt temperature and surface tension for Ti-6Al-4V does not allow the argon bubbles to escape. This feature is illustrated in a somewhat exaggerated form for reconstructed, 3D sections representing a range of melt scans: 1, 2, and 3 as shown in Figure 7a, b, and c, respectively. It is apparent that while the bubble distribution is not significantly altered with multiple melt passes, the microstructure is changed because of the variations in heat content and cooling rate. This is illustrated by the systematic increase in the acicular α -plate dimensions with the number of melt scans in Figure 7 a to c, respectively.

We have also recently shown that Ti-6Al-4V powders can be continuously recycled with no significant variation in elemental concentrations where Al concentrations averaged over hundreds of individual powder particles ranged from 4.3 to 7.3 weight percent Al and 2.9 to 3.8 weight percent V for the original (precursor) powder as illustrated for example in Figure 8 (Gaytan, et al., 2009). However, there was a notable variation in Al content for single melt pass monoliths versus three-melt pass monoliths: ranging from 10 to 15% for single and double melt pass (fully dense) monoliths (Figure 7a and b) in contrast to roughly 15 to 25% reduction in average Al content for triple (3) pass melt scans (Figure 7c). There was no systematic V loss between these melt scan/pass monoliths.

Thermal Management Microstructures and Mechanical Properties of Monolithic (Solid) and Complex Mesh Builds

It is apparent from Figure 7 that heat content and thermal management (cooling rate, etc.) can have a significant effect on the microstructure and associated mechanical behavior – such as residual hardness – for monolithic, solid products built by EBM. It has also been observed in this context that because heat content varies from the bottom to the top of a solid build—even for simple cylinders the microstructure and associated hardness will vary (Murr, et al. 2009a). Additionally, Murr, et al. (2009c) have recently demonstrated that complex mesh or open cellular structures can have variations in acicular α -phase platelets and α' -phase (hcp) platelets which produce a finer Widmanstätten structure, having higher residual hardness. Correspondingly, Murr, et al. (2009b) have shown that α' (martensite) phase platelets contribute to strengthening, but result in lower ductility (as measured by tensile elongation).

Figure 9 shows a CAD model and examples of actual builds for a 3D-reticulated mesh structure exhibiting non-isotropic hexahedral and octahedral (Figure 9c and d) geometrical arrays for a build element referred to as “dode-thin” from Materialize™ software (Murr et al. 2009c). These mesh arrays are composed of varying size struts or truss rods having diameters ranging from 0.5 to 1.5 mm, and with varying spacings which give rise to variations in residual, product porosities and densities as well as thermal or heat flow variations. Figure 10 shows an SEM view of these interconnected strut arrays along with a typical optical metallography view of the associated α' (martensite) platelets which can be contrasted with the variations in α -phase (hcp) acicular grains illustrated in Figure 7. Figure 11 shows for comparison the enlarged α -phase,

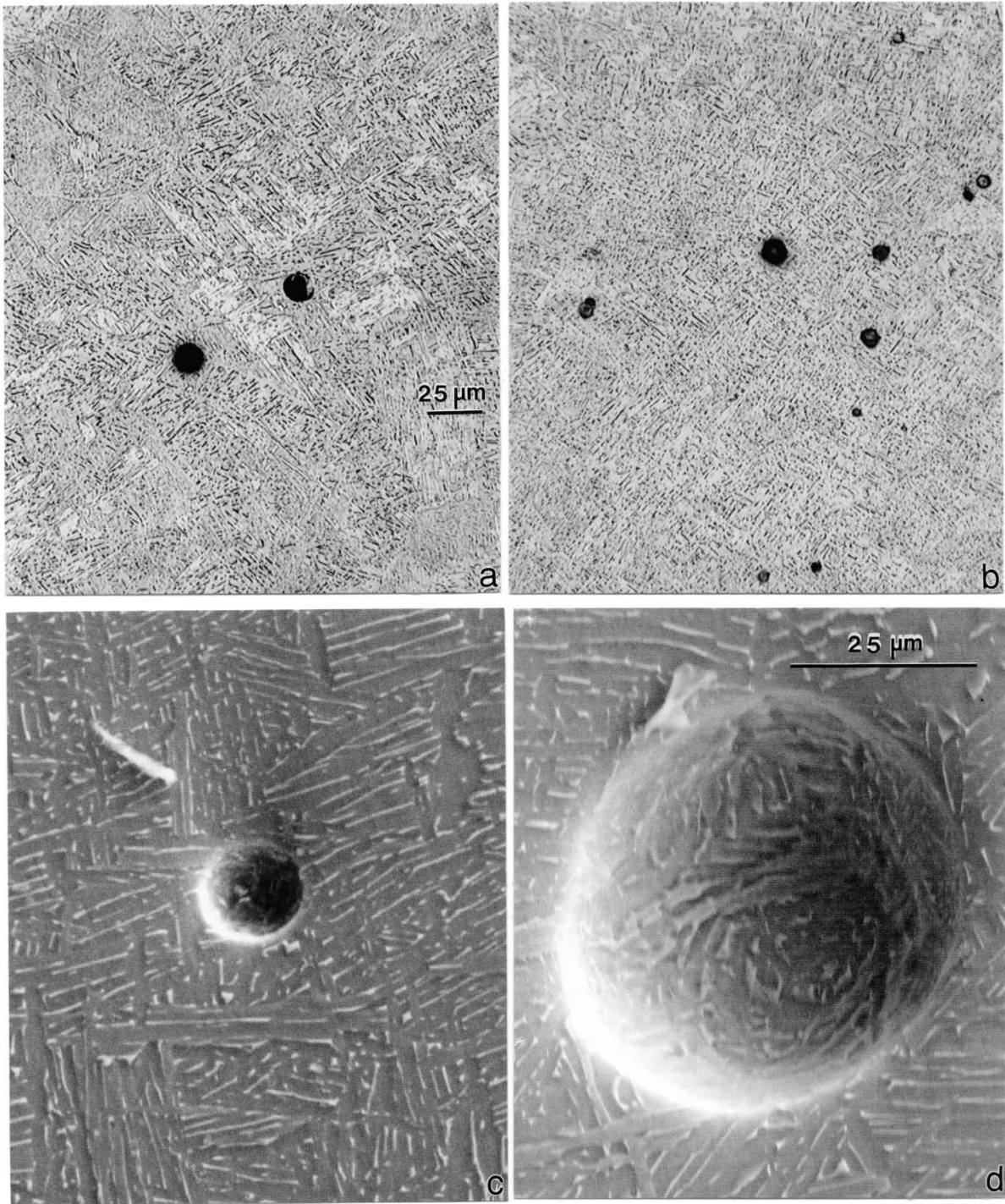


Figure 5. Examples of gas (void) bubbles in solid monoliths. (a) and (b) are optical metallograph images while (c) and (d) show SEM images.

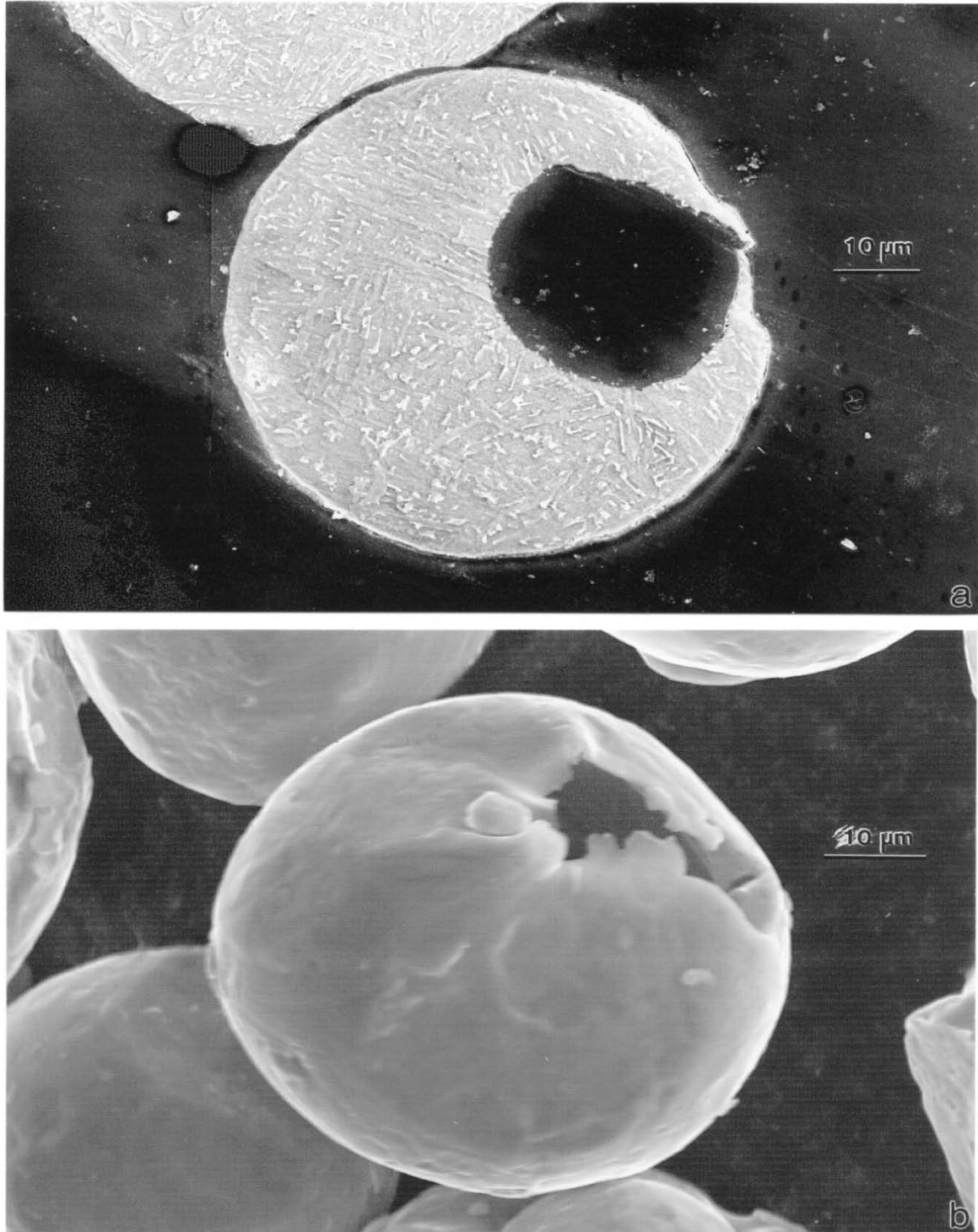


Figure 6. Gas bubbles in Ti-6Al-4V powders (typical for precursor/starting powder and recycled powder). (a) SEM metallographic view of mounted, ground, polished, and etched powder particle showing interior void. (b) SEM view of gas bubble breaking the powder particle surface. From Gaytan, et al. (2009).

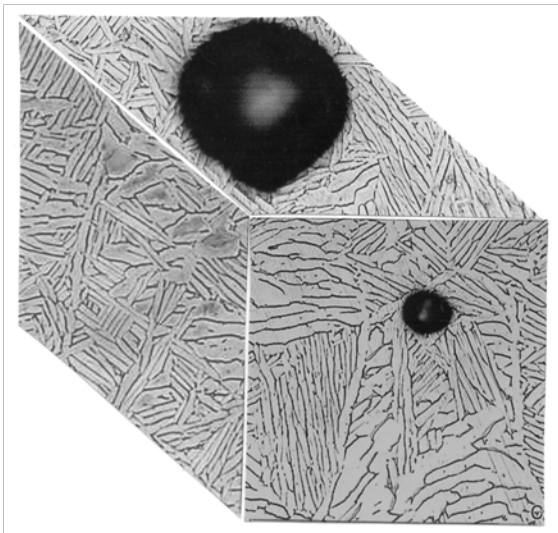
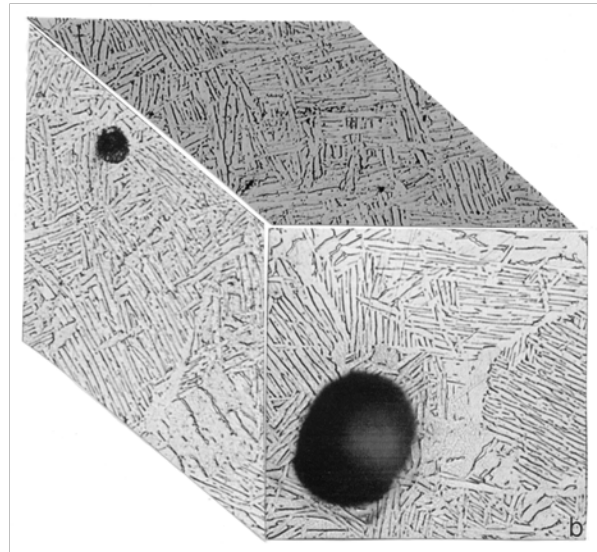
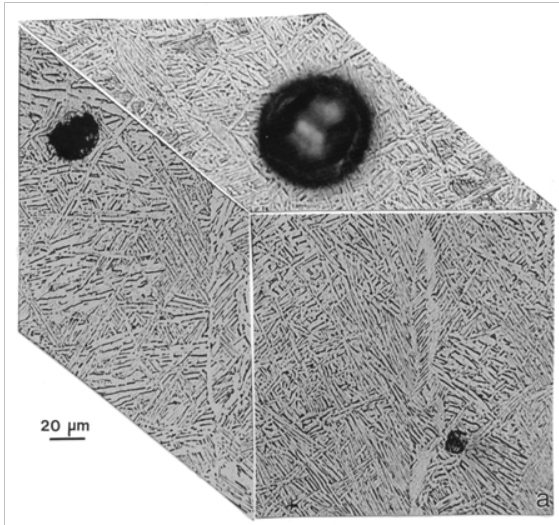


Figure 7. Series of 3D reconstructions of optical metallograph views for solid monoliths built with optimum melt scan parameters, but with (a) one melt scan, (b) two melt scans, (c) three melt scans. The bubble density is exaggerated in each case. Note variation in α -phase grain structure dimensions from (a) to (c). Magnifications the same as shown in (a).

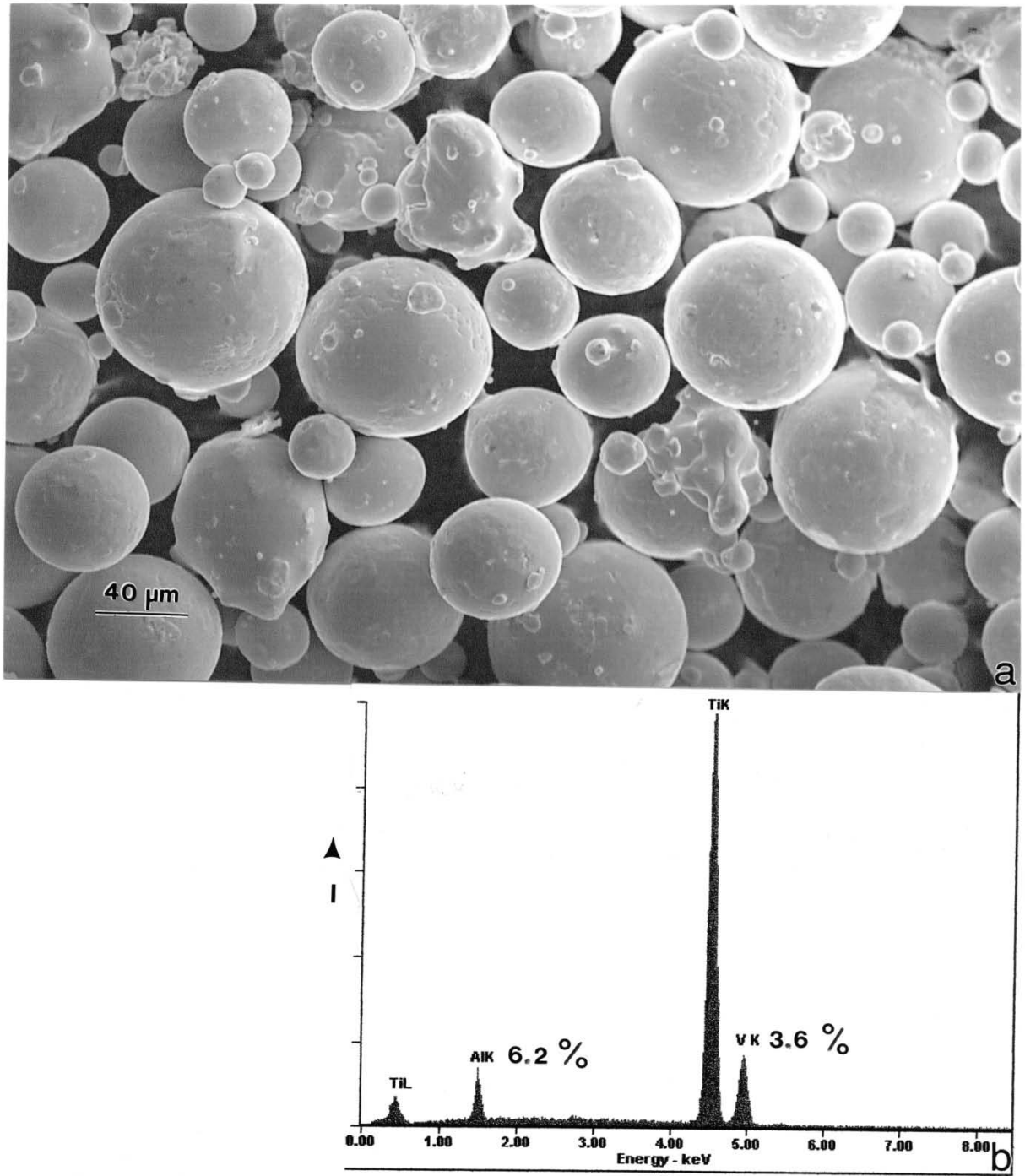


Figure 8. EDS analysis of individual powder particles after 10 cycles of mixed reuse (breakaway powder added to recycled powder). (a) SEM image of Ti-6Al-4V powder for comparison with the precursor powder insert in Figure 1. (b) EDS analysis of a single, random particle in (a). From Gaytan, et al. (2009).

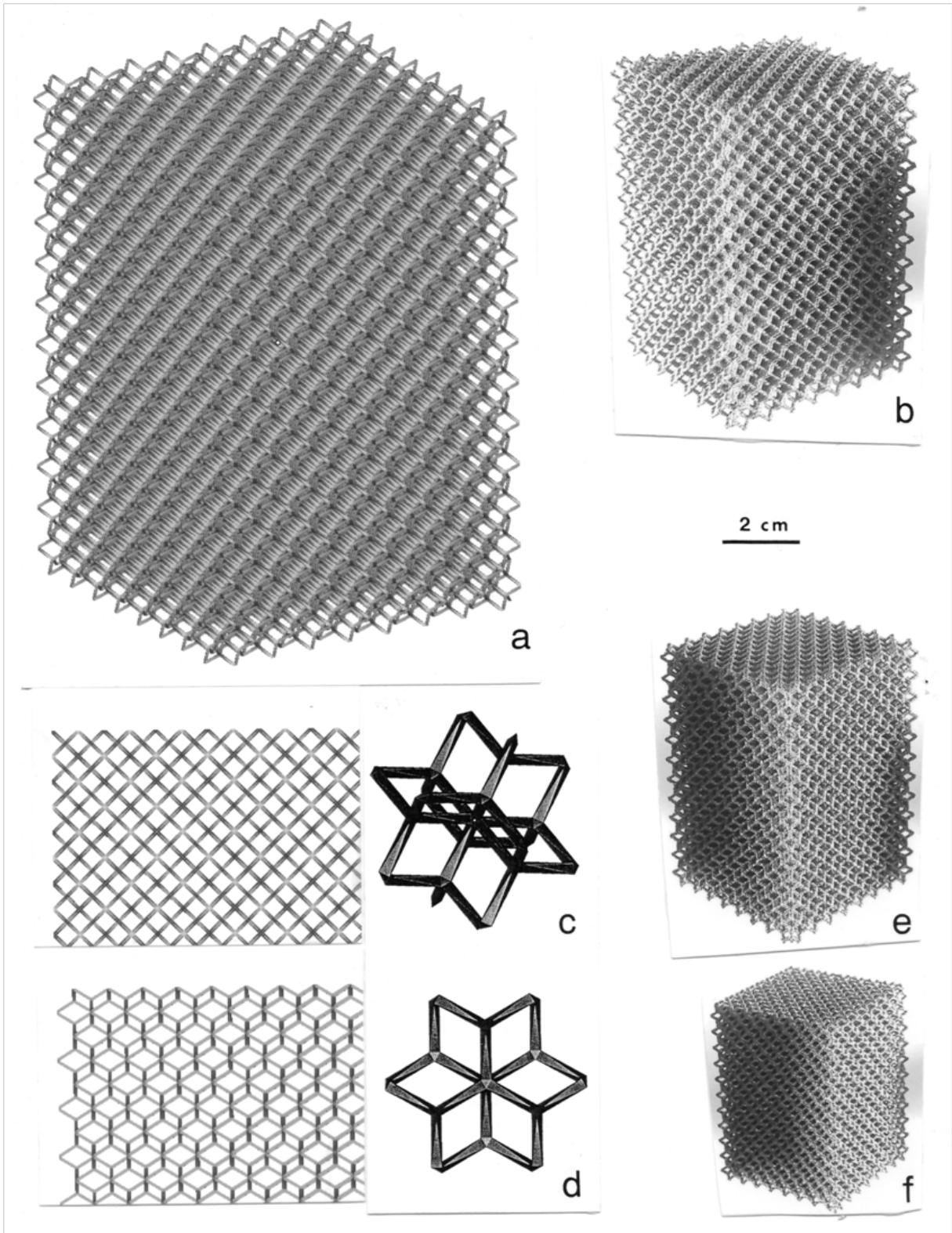


Figure 9. Software model views and EBM fabricated prototypes utilizing the Materialise™ dode-thin software element. (a) shows the software model while (b) shows the corresponding build. (c) and (d) show dode-thin element orientations which correspond to hexahedral and octahedral geometries occurring in the “faces” and diagonals (at 45°) in the structures. (e) and (f) show smaller mesh builds. From Murr, et al. (2009c).

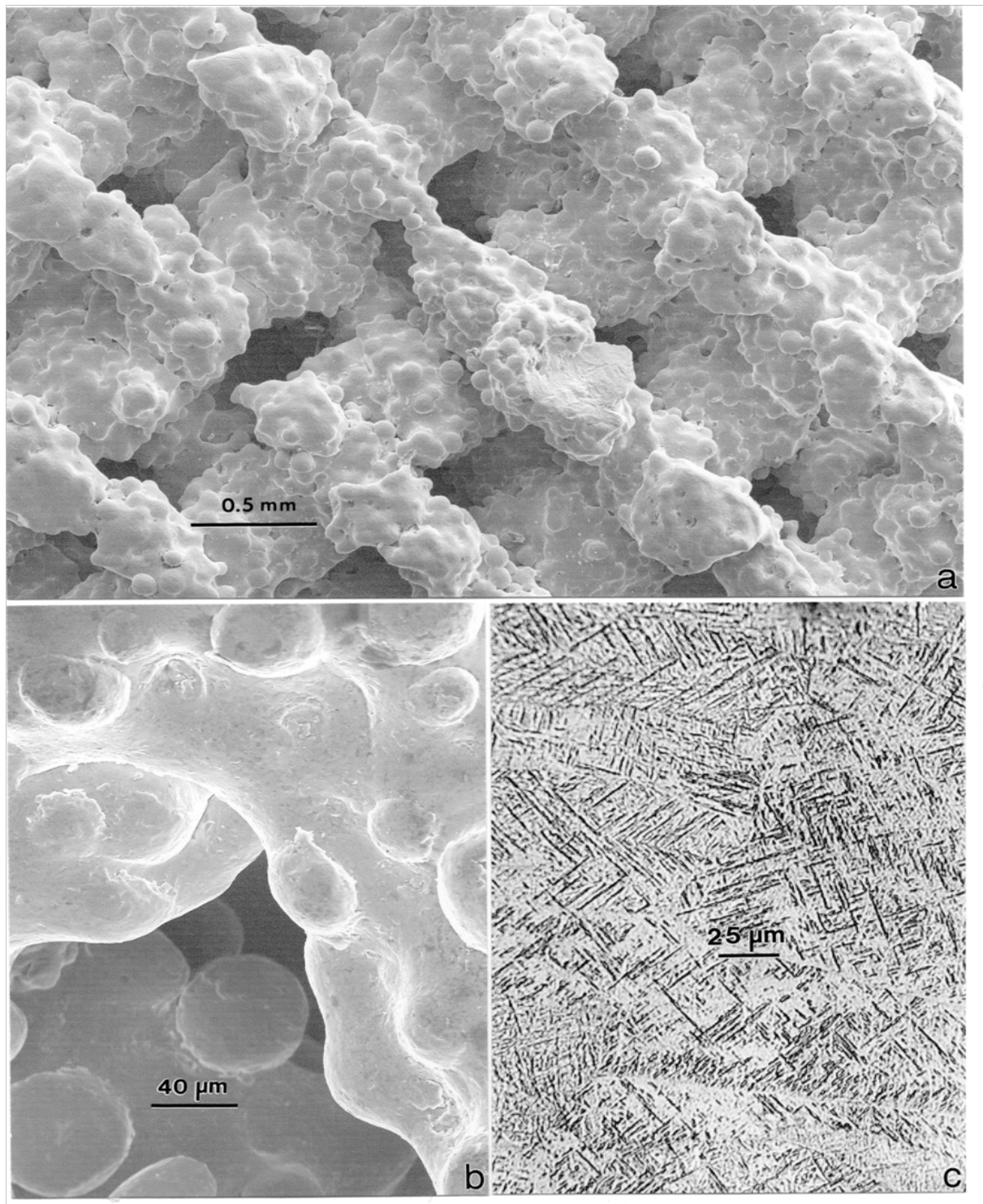


Figure 10. SEM and optical metallographic images of the dodecagonal mesh component in Figure 9(f). (a) Square (hexahedral) mesh geometry in SEM. (b) Magnified view of (a). (c) Optical microscopy image showing primarily α' martensite platelets intermixed with some α -phase on polished and etched connecting strut in (a). From Gaytan, et al. (2009).

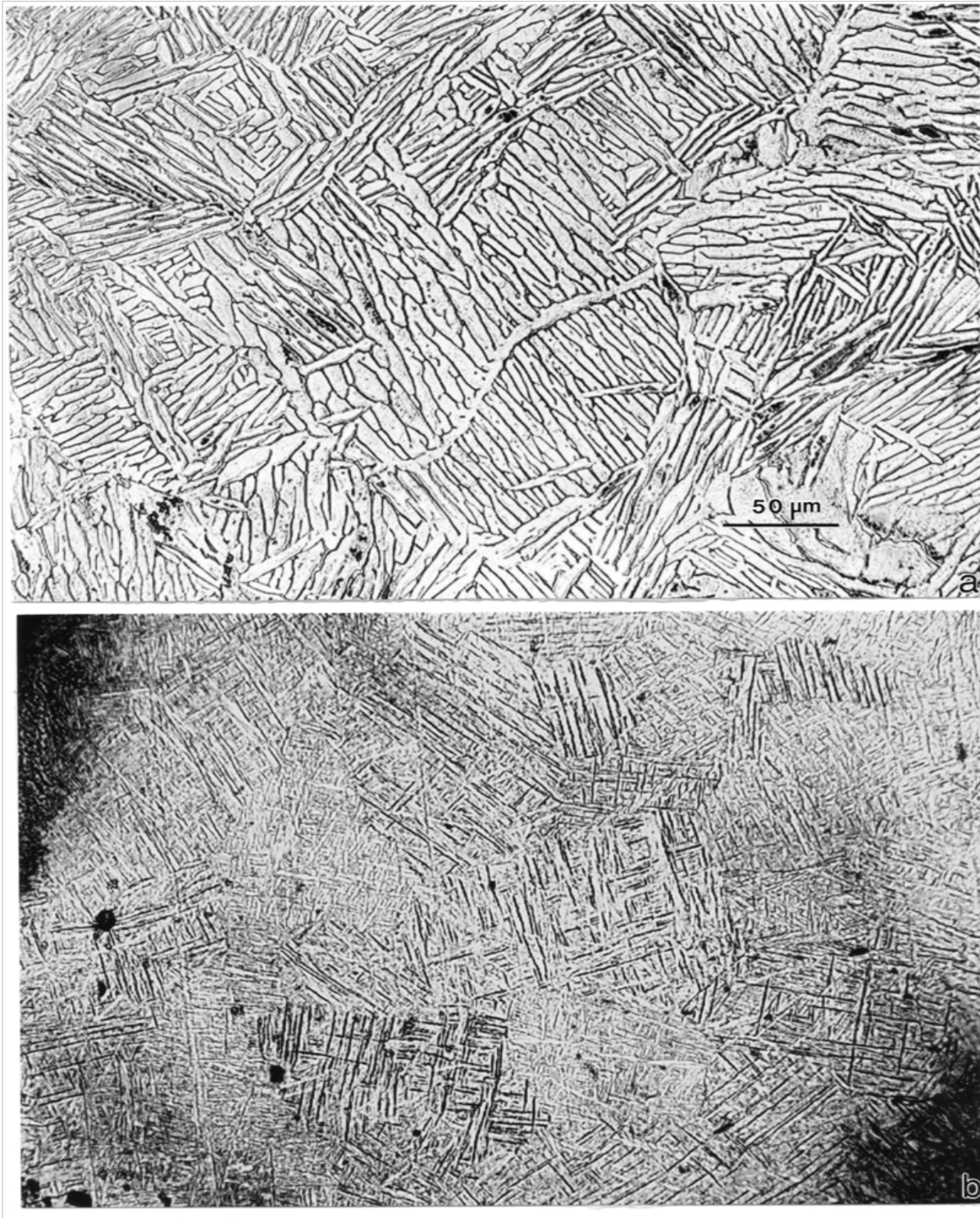


Figure 11. Comparison of residual microstructures for triple (3) melt pass fabrication of fully dense monolith in longitudinal plane (parallel to build direction) (a) with optimized single melt pass fabrication of 1.59 g/cm³ dense, Materialise™ dode-thin element strut (as in Figure 9(f)) showing primarily α' martensite platelets. From Murr, et al. (2009c).

acicular grain structure for a 3-melt pass (solid) build (Figure 11a) in contrast to the prominent α' (martensite) Widmanstätten microstructure in the mesh-strut structure corresponding to Figure 9(f).

Similarly, Figures 12 and 13 show several open cellular (foam) structures and their corresponding microstructures at different (higher) magnifications in the SEM. In Figure 13a, the cross-sections for the foam structure are roughly 1 mm in dimension while some structural units vary from 1 mm wide to 3 mm length. Note the layering implicit in the magnified SEM view shown in Figure 13b.

It might be expected that like the interconnected, small strut structures composing the mesh arrays illustrated in Figures 9 and 10, the cellular structures in Figure 12 and 13 would be expected to exhibit rapid cooling and some propensity of α' -martensite platelets. This feature is illustrated in Figure 14f in contrast to the α -phase platelet variation for increasing melt scans. (Figure 14a to c) and the variation of α -phase acicular grain structure from the top to the bottom of a simple, single melt scan cylindrical build shown respectively in Figure 14d and e.

Figure 15 compares the TEM microstructures which specifically correspond to the bottom, harder α -phase structure shown in Figure 14e (Figure 15a and b) and the 3-melt scan microstructures shown in Figures 7c, 11a, and 14c. The corresponding hardness difference from Figure 15 a and b to Figures 15 c and d represents a notable difference in dislocation density: $10^{10}/\text{cm}^2$ to $\sim 10^7$ - $10^8/\text{cm}^2$ comparing Figure 15b and Figure 15d, respectively.

Figure 16 illustrates the variance of β -phase (bcc) boundary prominence from more rapidly cooling components, and the appearance of the α' -martensitic phase comparing the “window” thicknesses implicit in experimental structures shown in Figure 2. In Figure 16b the α -phase boundaries are observed to be essentially free of β (bcc), while the contrast conditions show elongated dislocations within the α -phase. Figure 16a shows much less β -phase composing the boundary zones separating the α -phase in contrast to solid monolithic builds implicit in Figures 15a and c.

Finally, we should briefly discuss the mechanical behavior (including residual hardness and tensile properties) measured for a wide range of EBM-manufactured components: including variously built solid monoliths and mesh or foam structures. From the contrasting hardness values indicated in the various figure captions, it can be observed that the Vickers microindentation hardness for solid monoliths can vary from 3.6 GPa at the top (Figure 14d) to between 3.9 and 4.6 GPa at the bottom (Figure 14e) (Murr, et al. 2009a). Correspondingly, the average ultimate tensile strength (UTS) and corresponding elongations for solid cylinders have been shown to vary from roughly 1.1 GPa to 1.3 GPa and 12 to 25%, respectively (Murr, et al, 2009a). Figure 17 shows fracture surfaces corresponding to triple-melt-pass-built cylinders tested in tension to failure; with a UTS of ~ 1.1 GPa and an elongation of 12%. Note that the ductile dimple sizes vary from ~ 25 μm to 200 μm in diameter, in contrast to the bubble sizes shown in Figure 7c (as well as Figure 7 a and b) which vary from ~ 20 μm to <200 μm . Consequently there is little if any significance for these retained bubbles in initiating fracture.

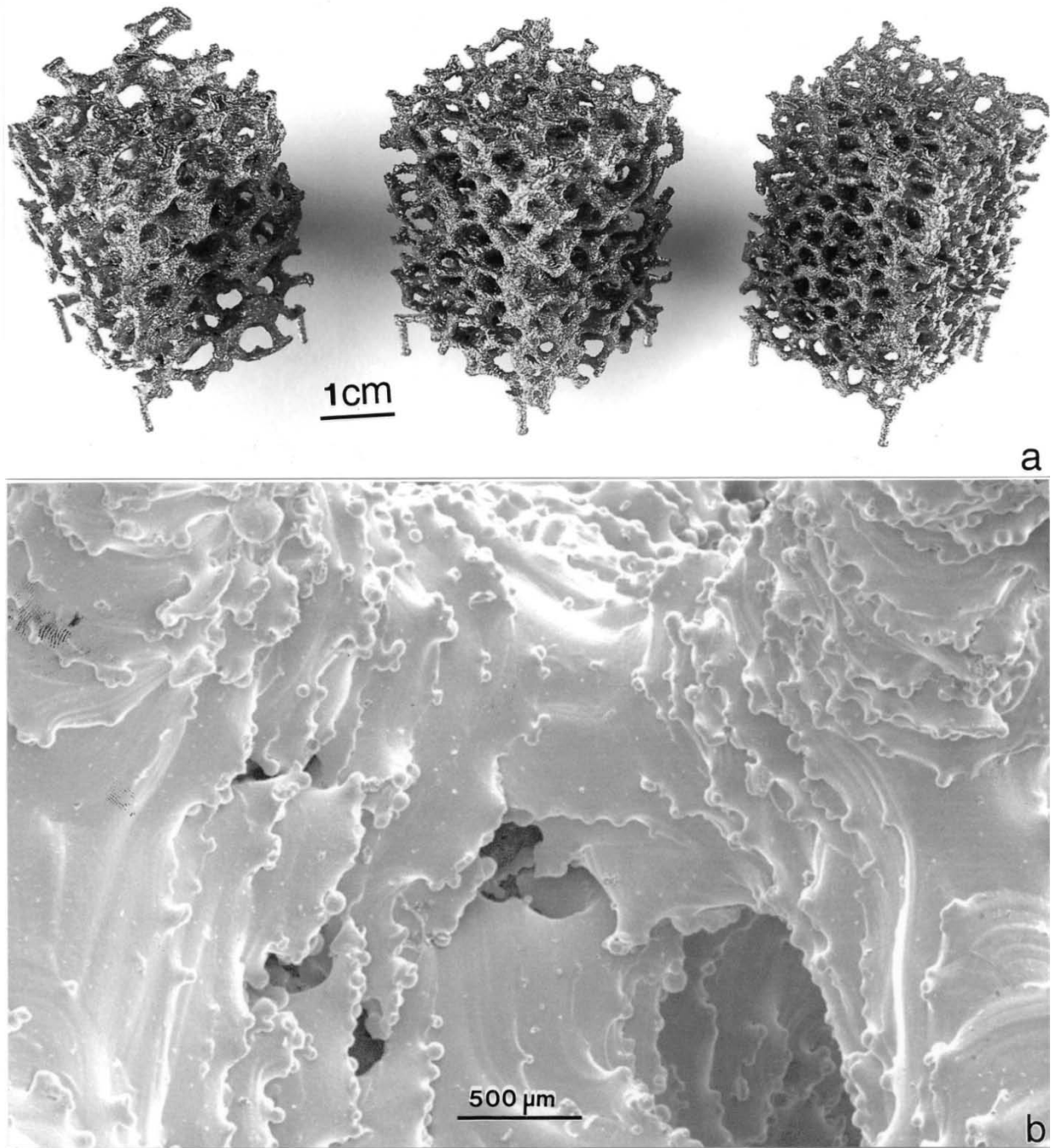


Figure 12. Three Ti-6Al-4V foam prototypes (a) and an SEM view of the center foam prototype (b). The foam prototypes in (a) correspond to (from left) 0.58, 0.68, and 0.83 g/cm³ densities, respectively.

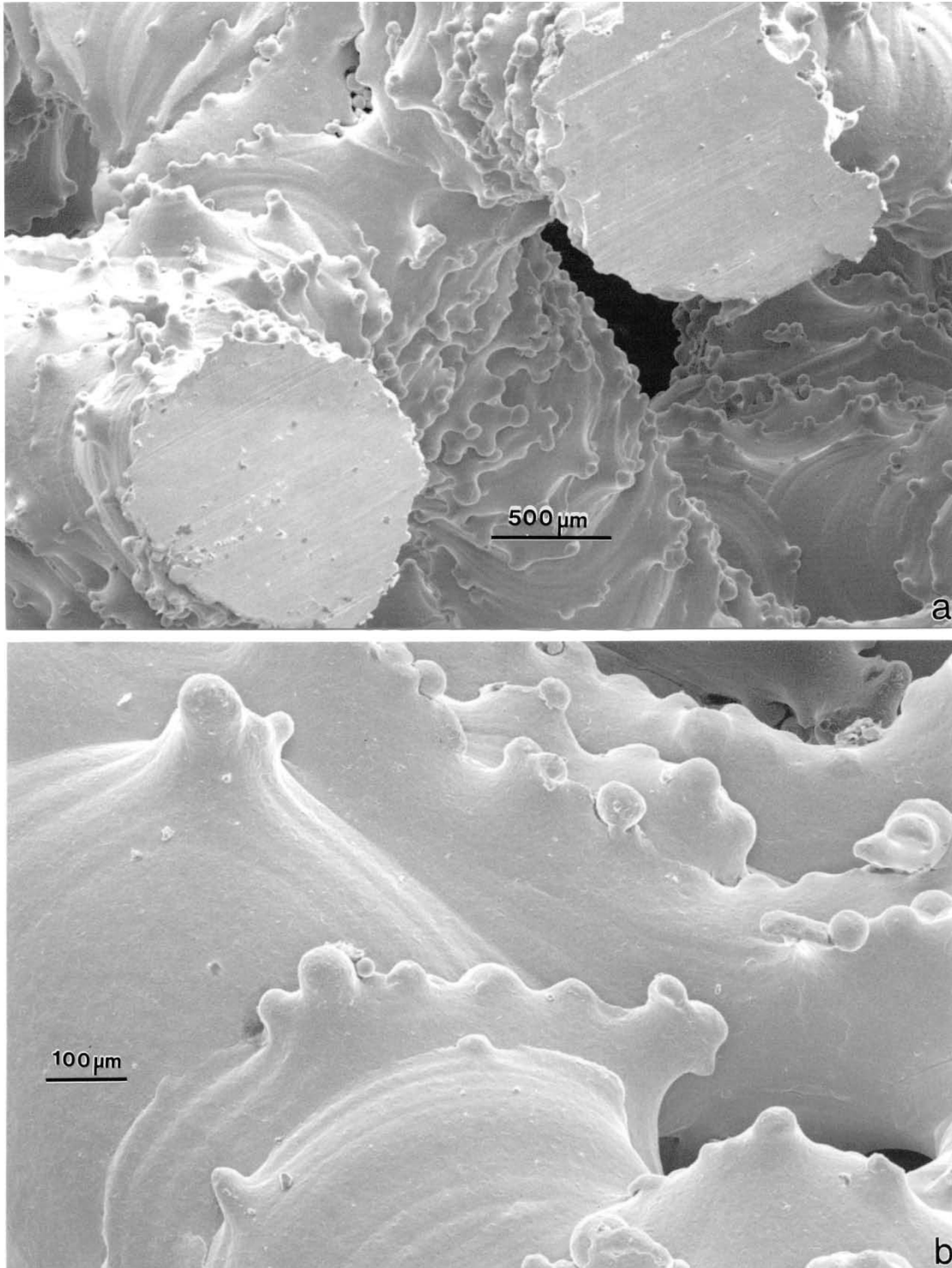


Figure 13. (a) SEM views of cut and polished cellular bridges in the center foam (0.68 g/cm^3) in Figure 12(a). (b) Magnified view of foam cells showing layering and edge-sintered powder particles.

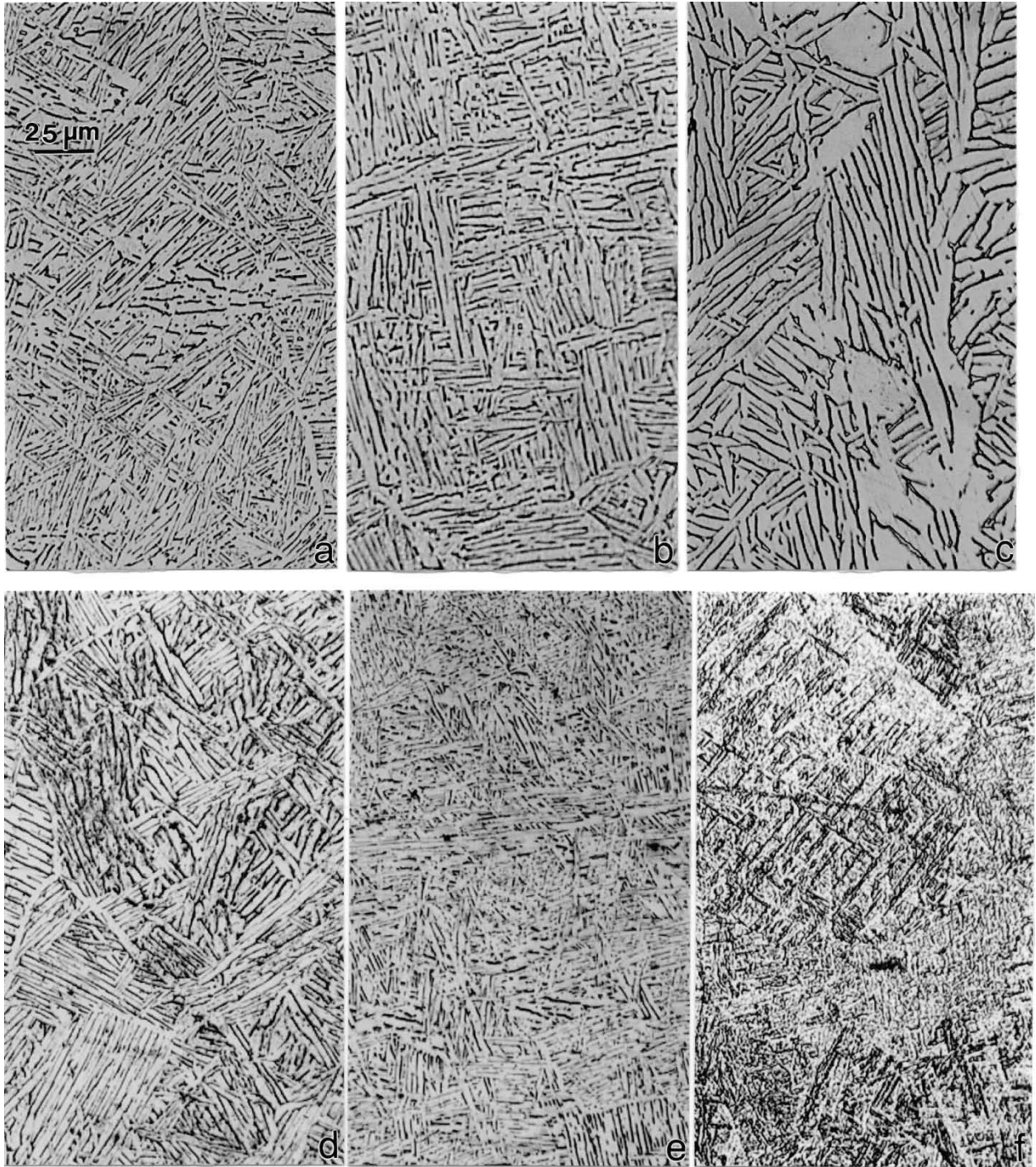


Figure 14. Optical metallographic views of microstructure variations resulting from thermal (cooling rate) variations. (a) to (c) show increasing α -phase, acicular grain dimension increases with increasing melt scans (from left: 1 scan, 2 scans, 3 scans, respectively). From Murr, et al. (2009c). (d) and (e) show α -phase variations from top (d) and bottom (e) sections of a 2 cm diameter, 5 cm long, fully dense cylinder. (f) shows a mix of α' martensite and α -phase platelets in a connecting strut in the cellular foam in Figure 12(b).

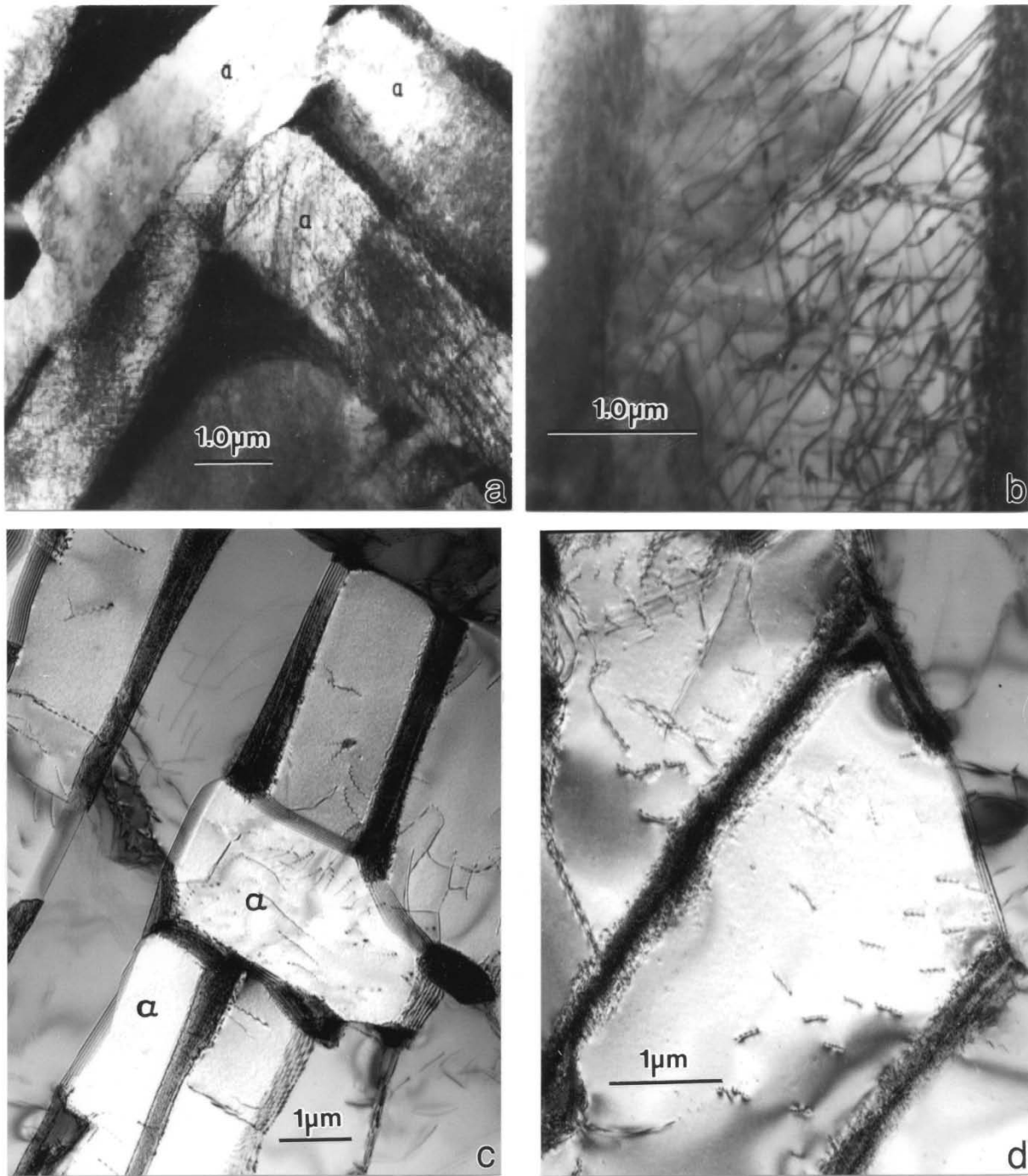


Figure 15. TEM bright-field image comparisons for single-melt-pass EBM fabrication of fully dense Ti-6Al-4V monoliths with variations in build thermal history to create dislocation density variations in the α -phase. (a) High hardness ($HV = 3.9 \text{ GPa}$), dislocation density $\sim 10^{10}/\text{cm}^2$. (b) Magnified view of dislocations in α -phase in (a). (c) Low hardness ($HV = 3.5 \text{ GPa}$), dislocation density $\sim 10^7/\text{cm}^2$. (d) Magnified view of region (c). From Murr, et al. (2009c).

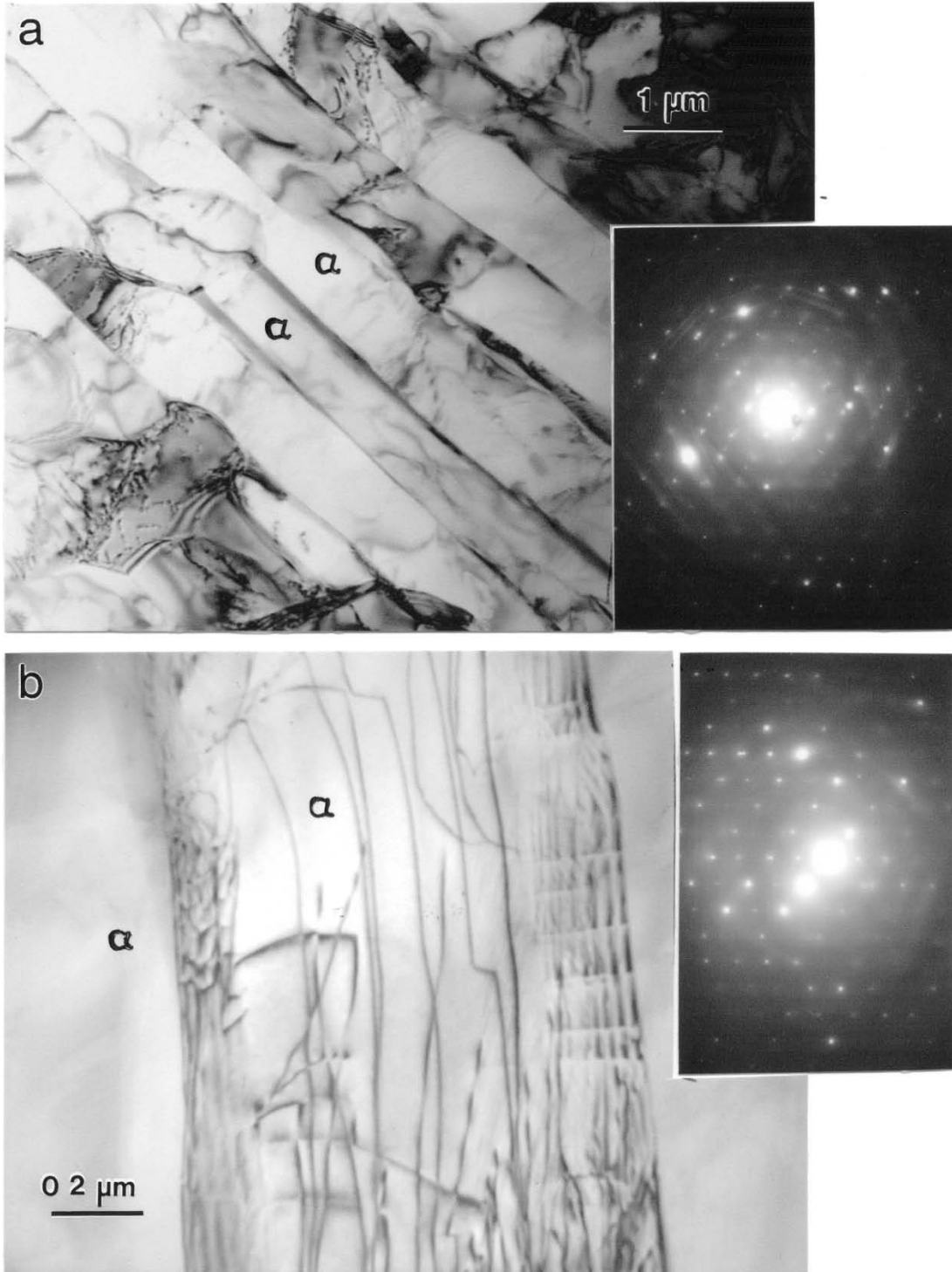


Figure 16. TEM bright-field image comparisons for (a) 0.91 mm thick “window” section corresponding to Figure 2(b), and (b) 0.64 mm thick “window” section corresponding to Figure 2(b). The selected-area electron diffraction pattern inserts show the same crystallographic orientation for (a) and (b).

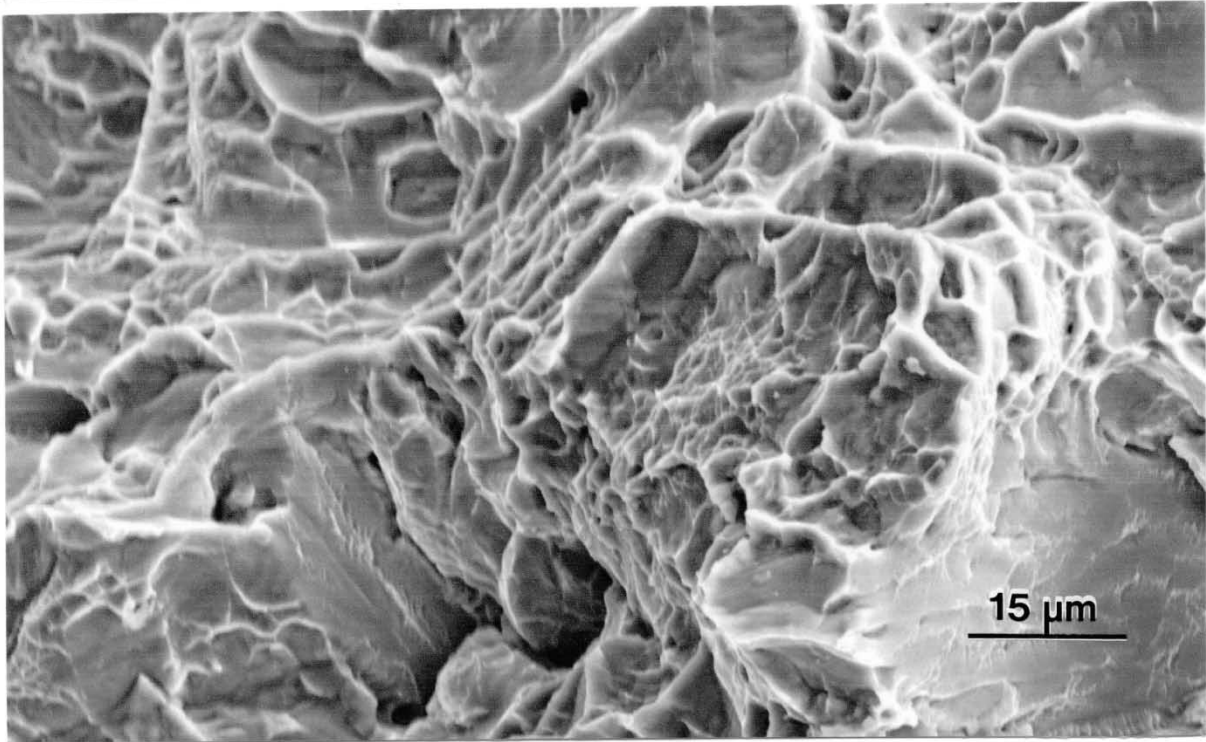
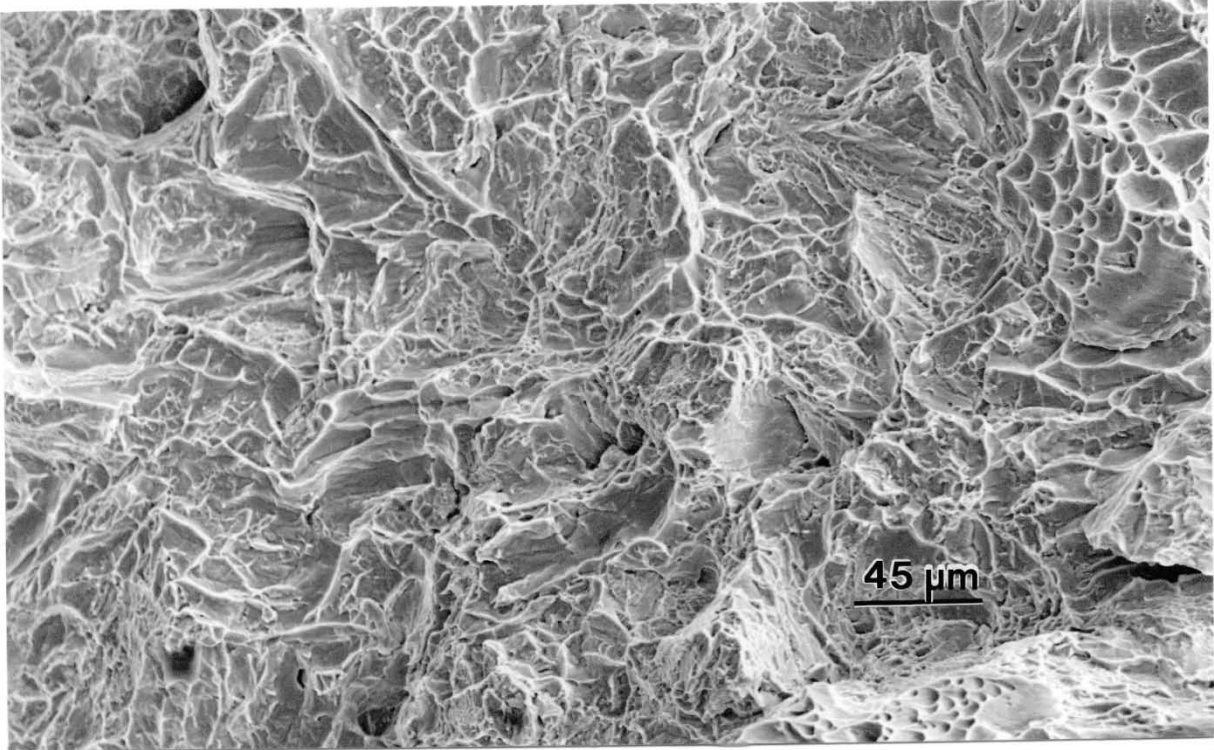


Figure 17. Low (a) and high (b) magnification SEM images of tensile specimen fracture surfaces. The specimen was machined from a triple (3) melt pass build of a 2 cm diameter, 8 cm long cylindrical specimen.

It can be noted that for the mesh and foam structures, the residual hardnesses exceed the nominal solid, monolith hardnesses (especially at the top of builds) by roughly 20%. Murr, et al. (2009b) observed that the UTS for α' -phase-rich tensile specimens prepared by selective laser melting (SLM) was equal to or slightly greater than the 1.1 GPa to 1.3 GPa noted earlier for EBM built α -phase monoliths, while the corresponding elongations were less than 10%, significantly lower than normal EBM-built solid monoliths. Recent measurements of the stiffnesses (elastic moduli) for mesh and foam structures varied with density, especially the mesh arrays shown in Figure 9, which ranged from a density of 0.78 g/cm³ and a stiffness of 0.92 GPa, to a density of 1.59 g/cm³, and a corresponding stiffness of 6.15 GPa (Murr, et al 2009c).

Conclusions

Build defects, including unmelted or unsintered powder regions can result from small deviations from optimum build parameters such as scan rate and beam current. No significant difference in build integrity has been observed for single rake versus double/triple rake layer building, while changing from one to three melt scans at optimized build conditions produces increasing α -phase microstructure dimensions and corresponding decreases in residual hardness. It is also observed that in solid, monolithic builds, there is a larger α -phase grain size at the top of the build in contrast to the bottom of the build, and corresponding residual hardness differences (higher hardness at the build bottom versus lower hardness at the top of the build). This results by thermal management differences (or cooling rate variations). Correspondingly, for rapid cooling rates characteristic of small, reticulated mesh arrays and open cellular foams, the microstructures tend toward α' -martensitic platelets which are correspondingly harder than the α -phase acicular platelets as a consequence of their smaller thickness. Argon bubbles carried into the build from the atomized precursor Ti-6Al-4V powders do not appear to vary with increasing melt scans nor do they noticeably influence the tensile behavior of solid monoliths as observed by fracture surface features dominated by varying sizes of ductile dimples.

Acknowledgements

This research was supported in part by Mr. and Mrs. MacIntosh Murchison Chair endowments at the University of Texas at El Paso and Lockheed Martin/Aeronautics. Any expressed opinions, findings, conclusions, or recommendations are those of the authors, and do not necessarily represent those of Lockheed Martin/Aeronautics.

References

- Gaytan, S.M., Murr, L.E., Medina, F., Martinez, E., Lopez, M.I., and Wicker, R.B. (2009). Advanced metal powder-based manufacturing of complex components by electron beam melting. *Materials Technology*, in press.
- Murr, L.E., Esquivel, E.V., Quinones, S.A., Gaytan, S.M., Lopez, M.I., Martinez, E.Y., Medina, F., Hernandez, D.H., Martinez, E., Stafford, S.W., Brown, D.K., Hoppe T., Meyers, W., Lindhe, U. and Wicker, R.B. (2009a). Microstructures and mechanical properties of electron beam-rapid manufactured Ti-6Al-4V biomedical prototypes compared to wrought Ti-6Al-4V. *Materials Characterization*, **60**: 96-105.
- Murr, L.E., Quinones, S.A., Gaytan, S.M., Lopez, M.I., Rodela, A., Martinez, E.Y., Hernandez, D.H., Martinez, E., Medina, F., and Wicker, R.B. (2009b). Microstructure and mechanical behavior of Ti-6Al-4V produced by rapid-layer manufacturing for biomedical applications. *Journal of Mechanical Behavior of Biomedical Materials*, **2**: 20-32.

Murr, L.E., Gaytan, S.M., Medina, F., Lopez, H., Martinez, E., Machado, B.I., Hernandez, D.H., Martinez, L., Lopez, M.I., Wicker, R.B., Bracke, J. (2009c). Next generation biomedical implants using additive manufacturing of complex, cellular and functional mesh arrays. Philosophical Transactions A (Royal Society, London), in press.

Wooten, J. (2008). Electron beam melting manufacturing of flight hardware for the Navy UCAS program. Paper presented at SAE meeting in South Carolina, Oct, 2008. Contact <johnwooten1877@att.ent>.